Chinese Journal of Aeronautics, (2015), 28(4): 1178–1188

Chinese Society of Aeronautics and Astronautics
& Beihang University

Chinese Journal of Aeronautics

cja@buaa.edu.cn
www.sciencedirect.com

An improved imaging algorithm for spaceborne MAPs sliding spotlight SAR with high-resolution wide-swath capability

Kuang Hui [a], **Chen Jie** [a], **Yang Wei** [a,*], **Liu Wei** [b]

[a] *School of Electronic and Information Engineering, Beihang University, Beijing 100191, China*
[b] *Electronic and Electrical Engineering Department, University of Sheffield, Sheffield S1 3JD, UK*

Received 1 November 2014; revised 2 January 2015; accepted 9 February 2015
Available online 19 June 2015

KEYWORDS

High resolution;
Imaging;
Multiple-azimuth-phases;
Sliding spotlight;
Synthetic aperture radar;
Wide swath

Abstract Conventional synthetic aperture radar (SAR) systems cannot achieve both high-resolution and wide-swath imaging simultaneously. This problem can be mitigated by employing multiple-azimuth-phases (MAPs) technology for spaceborne sliding spotlight SAR systems. However, traditional imaging algorithms have met challenges to process the data accurately, due to range model error, MAPs data reconstruction problem, high-order cross-coupling phase error and variation of Doppler parameters along the azimuth direction. Therefore, an improved imaging algorithm is proposed for solving the above problems. Firstly, a modified hyperbolic range equation (MHRE) is proposed by introducing a cubic term into the traditional hyperbolic range equation (THRE). And two curved orbit correction methods are derived based on the proposed range model. Then, a MAPs sliding spotlight data reconstruction method is introduced, which solves the spectral aliasing problem by a de-rotation operation. Finally, high-order cross-coupling phases and variation of Doppler parameters are analyzed and the corresponding compensation methods are proposed. Simulation results for point-target scene are provided to verify the effectiveness of the proposed algorithm.

1. Introduction

In the past decades, significant progress has been made in remote sensing with the aid of spaceborne synthetic aperture radar (SAR). To meet the needs of specific applications and also improve the performance of spaceborne SAR systems, different imaging modes have been developed, such as stripmap, ScanSAR, spotlight, sliding spotlight, TOPS (terrain observation by progressive scan) and inverse TOPS.[1–4] However, many of them are incapable of imaging wide swath with high

* Corresponding author. Tel.: +86 10 82338670.
E-mail address: yangweigigi@sina.com (W. Yang).

Peer review under responsibility of Editorial Committee of CJA.

Production and hosting by Elsevier

http://dx.doi.org/10.1016/j.cja.2015.06.009

geometric resolution. This problem can be solved by employing multiple-azimuth-phases (MAPs) technology in sliding spotlight mode, which will be implemented in TerraSAR-X2 in the future and is named as multiple-azimuth-phases very-high-resolution (MAPs-VHR) sliding spotlight mode.[5]

Several factors should be considered for high-resolution wide-swath (HRWS) imaging. Firstly, traditional imaging algorithms are derived based on the straight trajectory assumption, which leads to un-negligible phase error for high-resolution SAR systems. Therefore, the phase error caused by a curved orbit should be compensated in some ways. Secondly, as for the MAPs-VHR sliding spotlight mode, to obtain a wide swath, the pulse repetition frequency (PRF) is selected to be less than the Doppler bandwidth, resulting in spectral aliasing in azimuth direction. As a result, different from MAPs stripmap data reconstruction, MAPs-VHR sliding spotlight data should be reconstructed with under-sampling. Thirdly, with high-resolution and wide-swath, high-order cross-coupling phases between azimuth and range become so large that they should be compensated too, especially for targets at the edge of the scene. At last, Doppler parameters vary slightly along azimuth direction due to rotation of Earth and curved orbit. This variation cannot be ignored in high-resolution systems.

With the above considerations, several methods have been proposed. In Ref.[6], a numerical method is presented for compensating the error caused by a curved orbit. However, this method cannot guarantee image quality at the edge of the scene. An advanced hyperbolic range equation (AHRE) is proposed to describe the curved orbit for medium-Earth-orbit (MEO) in Ref.[7], which only performs well for medium/low-resolution spaceborne SAR systems. For the high resolution case, two methods are described to compensate the curved orbit error in Ref.[8], by applying corrections in the azimuth frequency domain and azimuth time domain, respectively. A novel fourth-order Doppler range model (DRM4) is proposed for high-resolution LEO SAR in Ref. [9], which needs to utilize fourth-order Doppler parameters. To overcome the spectral aliasing problem in monostatic sliding spotlight SAR, a modified deramp chirp scaling algorithm (MDCS) is proposed in Ref.[10] Compared with the two-step algorithm for spotlight SAR data processing in Ref.[11], a de-rotation operation is implemented in the first step. But the MDCS algorithm ignores the azimuth re-sampling effect caused by de-rotation operation, which may result in image aliasing in azimuth direction. A baseband azimuth scaling (BAS) algorithm is derived in Ref.[12], based on the extended chirp scaling (ECS) algorithm.[13] It can avoid spectral aliasing in azimuth direction by adding a post-processing step. However, as a sub-aperture algorithm, spectrum splitting is needed for BAS algorithm, leading to strict requirements on phase preserving accuracy. Contrary to the BAS algorithm, a three-step full-aperture algorithm is proposed in Ref.[14], where a de-rotation operation is performed first to avoid data division, followed by a deramp operation to avoid image aliasing. For MAPs SAR systems, the data should be reconstructed first using methods proposed in Ref.[15–17]. However, such methods are based on the condition that the total Doppler bandwidth should be smaller than the equivalent PRF, which cannot be satisfied in MPAs-VHR sliding spotlight SAR system. In Ref.[18], a novel "staircase" method is presented to reconstruct the MPAs TOPS SAR data, which can be adopted for the MPAs sliding spotlight mode.[19] But the "staircase" method needs to split the raw data into sub-aperture in azimuth direction, thus an additional sub-aperture combining operation has to be applied in azimuth frequency domain, which is only suitable for sub-aperture imaging algorithms. To solve the problem, full aperture azimuth processing for MPAs Beam Steering SAR (BS-SAR) is proposed in Ref.[20], based on beam compression and azimuth bandwidth compression of signals in the Doppler-array and slow time-angle planes, which is a very complicated process.

Based on the above analysis, a refined three-step algorithm is proposed in this paper for accurately processing MAPs-VHR sliding spotlight SAR data. In order to describe the curved orbit more accurately, a modified hyperbolic range equation (MHRE) is presented firstly, which adds a cubic term into the traditional hyperbolic range equation (THRE). Two methods for compensating the curved orbit error are derived based on the MHRE. Then, a reconstruction method for MPAs-VHR sliding spotlight SAR data is introduced, which contains three main steps, including Dechirp Operation, Filter Operation, and Rechirp Operation. This method can perform reconstruction and de-rotation operations simultaneously. After data reconstruction, the spectrum in azimuth is no longer aliased and frequency focusing algorithms can be applied. Furthermore, high-order cross-coupling phases between range and azimuth are analyzed and a corresponding compensation method is provided. Variation of Doppler parameters along the azimuth direction is considered during data processing. The effectiveness of our proposed method is verified by extensive simulations.

This paper is organized as follows. Section 2 reviews the MPAs-VHR sliding spotlight mode based on the MHRE and discusses the signal property. Section 3 addresses the derivation of MPAs-VHR sliding spotlight SAR data processing algorithm, including MAPs data reconstruction, curved orbit correction, high-order cross-coupling phases compensation and Doppler parameters updating along azimuth. Imaging results of simulated point targets are given in Section 4 to validate the proposed focusing algorithm, and conclusions are drawn in Section 5.

2. MPAs-VHR sliding spotlight mode

The MPAs-VHR sliding spotlight mode is proposed for high resolution and wide swath imaging. In this section, imaging geometry of the proposed mode is reviewed based on MHRE and the signal characteristic is analyzed in detail.

2.1. Imaging geometry

Imaging geometry of the MPAs-VHR sliding spotlight mode is shown in Fig. 1, where v_s is the velocity of the satellite, v_g the velocity of the beam center on the ground, O the center of the scene, O' the rotation center of the azimuth antenna-beam which is located at a point below the scene surface, R_{rs} the closest distance between the rotation center and the satellite and r the slant range. For sliding spotlight mode, the azimuth antenna-beam sweeps back and forth to extend the illumination time to achieve high azimuth resolution. Moreover, the MPAs technology is applied to reducing PRF for a wide swath image. The hybrid factor $Y(r)$ is defined by

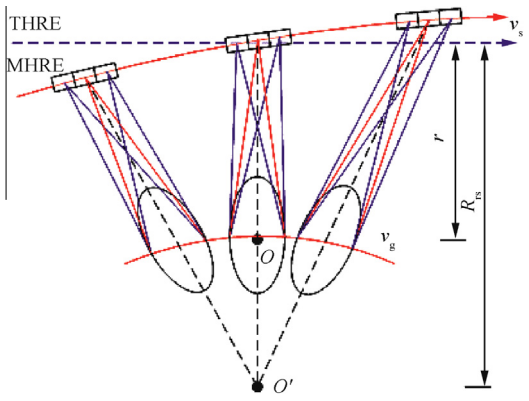

Fig. 1 Imaging geometry of MPAs-VHR sliding spotlight mode.

$$Y(r) = \frac{R_{rs} - r}{R_{rs}} \tag{1}$$

2.2. MHRE

The THRE is used by most spaceborne SAR processors, which assumes that the trajectory of the sensor is a straight line. In practice, the trajectory of the satellite is curved based on the Keplerian orbit. The straight trajectory assumption becomes less accurate as the aperture time becomes longer, especially when the resolution is higher than 0.5 m. In Ref.[21], THRE is given by

$$R(t;r) = \sqrt{r^2 + (v_r t)^2 - 2 r v_r t \cos\varphi_{eq}} \tag{2}$$

where t is azimuth time, φ_{eq} equivalent angle, and $v_r \approx \sqrt{v_s v_g}$ effective radar velocity.[22] To describe the satellite orbit more accurately, in this paper, an additional cubic coefficient $\frac{\lambda}{6}\gamma(r)$ is introduced into the THRE to form the MHRE model

$$R(t;r) = \sqrt{r^2 + (v_r t)^2 - 2 r v_r t \cos\varphi_{eq}} + \frac{\lambda}{6}\gamma(r) t^3 \tag{3}$$

where λ is carrier wavelength and $\gamma(r)$ is relative to the slant range and there is no analytic expression for it. Thus, it needs to be estimated by numerical approaches for every image scene.

2.3. Signal mode

The signal of a point target at azimuth time $t = 0$ and slant range r for the ith receive channel can be described as

$$\begin{aligned} S_i(\tau,t;r) = {} & \sigma \cdot \mathrm{rect}\left\{\frac{1}{T_p}\left[\tau - \frac{1}{c}\left(R(t;r) + R\left(t - \frac{d_i}{v_r};r\right)\right)\right]\right\} \\ & \cdot \mathrm{rect}\left(\frac{Y(r) v_r t}{X}\right) \cdot \mathrm{rect}\left(\frac{t}{T_{scene}}\right) \\ & \cdot \exp\left[-\mathrm{j}2\pi k\left(\tau - \frac{R(t;r) + R\left(t - \frac{d_i}{v_r};r\right)}{c}\right)^2\right] \\ & \cdot \exp\left[-\mathrm{j}2\pi \frac{R(t;r) + R\left(t - \frac{d_i}{v_r};r\right)}{\lambda}\right] \end{aligned} \tag{4}$$

where σ represents the target cross-section, τ range time , $X \approx \lambda r / L$ the azimuth antenna footprint, L the length of antenna, T_{scene} the azimuth integration time, c the speed of light, k the FM rate of the transmitted chirp pulse, d_i the along-track displacement of the ith receive channel center relative to the transmitter channel center, $R(t;r)$ the slant range between the transmitter channel center and the target point, and $R\left(t - \frac{d_i}{v_r};r\right)$ the slant range between the target point and the i th receive channel center.

Fig. 2 shows the time–frequency diagram of the sliding spotlight mode, f_t is azimuth frequency ,k_r and k_w represent Doppler rate and antenna sweep rate, respectively, given by

$$\begin{cases} k_r = \dfrac{2 v_r^2 \cos^2\varphi_{eq}}{\lambda r} \\ k_w = \dfrac{2 v_r^2 \cos^2\varphi_{eq}}{\lambda R_{rs}} \end{cases} \tag{5}$$

$B_{3\,dB}$ represents 3 dB Doppler bandwidth, and B_{steer} the Doppler bandwidth resulting from azimuth antenna-beam steering, which can be written as

$$B_{steer} = |k_w| T_{scene} \tag{6}$$

The total Doppler bandwidth $B_{total} = B_{3dB} + B_{steer}$ is much larger than the equivalent pulse repetition frequency $M \cdot \mathrm{PRF}$, where M denotes the number of azimuth receive channels.

3. MPAs-VHR SAR processing algorithm

This section considers several specific aspects for processing the MAPs-VHR spaceborne sliding spotlight SAR data. For each aspect, a corresponding solution is provided. Then, an algorithm is proposed based on the overall analyses.

3.1. MPAs data reconstruction

For MPAs-VHR sliding spotlight mode, as the Doppler bandwidth is much larger than the equivalent PRF, MPAs data reconstruction should be applied with azimuth undersampling. Similar to the MPAs stripmap mode, the characteristics of the signal in azimuth are analyzed first. Eq. (4) can be simplified as follows, which only considers the azimuth signal

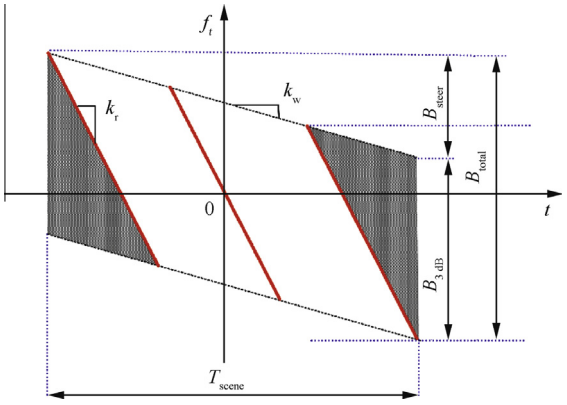

Fig. 2 Time–frequency diagram of sliding spotlight mode.

$$h_i(t;r) = \sigma \cdot \mathrm{rect}\left(\frac{Y(r)v_r t}{X}\right) \cdot \mathrm{rect}\left(\frac{t}{T}\right) \cdot \exp\left[-\mathrm{j}\frac{2\pi}{\lambda}\left(R(t;r) + R\left(t - \frac{d_i}{v_r};r\right)\right)\right] \quad (7)$$

Expanding Eq. (3) using Taylor series up to the second order yields

$$h_i(t;r) \approx \sigma \cdot \mathrm{rect}\left(\frac{Y(r)v_r t}{X}\right) \cdot \mathrm{rect}\left(\frac{t}{T}\right) \cdot \exp\left[-\mathrm{j}\frac{2\pi}{\lambda}\left(2R\left(t - \frac{d_i}{2v_r};r\right) + \frac{k_r d_i^2}{8v_r^2}\right)\right] \quad (8)$$

Thus, the transfer function $H_i(f_t)$ between the transmitter and the ith receiver with respect to the monostatic impulse response is given by [15]

$$H_i(f_t) = \exp\left(-\mathrm{j}\frac{\pi k_r d_i^2}{4v_r^2}\right) \cdot \exp\left(-\mathrm{j}2\pi f_t \frac{d_i}{2v_r}\right) \quad (9)$$

where $-M \cdot \mathrm{PRF}/2 \leqslant f_t \leqslant M \cdot \mathrm{PRF}/2$. Note that the phase offset $\frac{\pi k_r d_i^2}{4v_r^2}$ is variant corresponding to azimuth time with the steering of azimuth antenna beam, leading to modulation in azimuth, which may degrade image quality when it is large. Fortunately, the phase offset variation is normally smaller than 0.1° and therefore can be ignored. [18] However, in order to guarantee an acceptable image quality, the residual phase offset is compensated as well. Based on the transfer function $H_i(f_t)$ for every channel, the reconstructed filters $P_i(f_t)$ can be obtained with the method in Ref.[15]

With the reconstructed filter, an MPAs data reconstruction method is proposed based on the de-rotation operation. [14] The method contains three main steps, including dechirp operation, filter operation and rechirp operation, as shown in Fig. 3, and the detailed operations are described as follows.

(1) Dechirp operationThe dechirp operation can be realized by multiplying the i th channel signal $S_i(t,\tau;r)$ with the corresponding dechirp filter $H^i_{\mathrm{dechirp}}(t)$.

$$H^i_{\mathrm{dechirp}}(t) = \exp\left[\mathrm{j}\pi k_w (t - t^i_{\mathrm{del}})^2 + \mathrm{j}\pi f_d (t - t^i_{\mathrm{del}})\right] \quad (10)$$

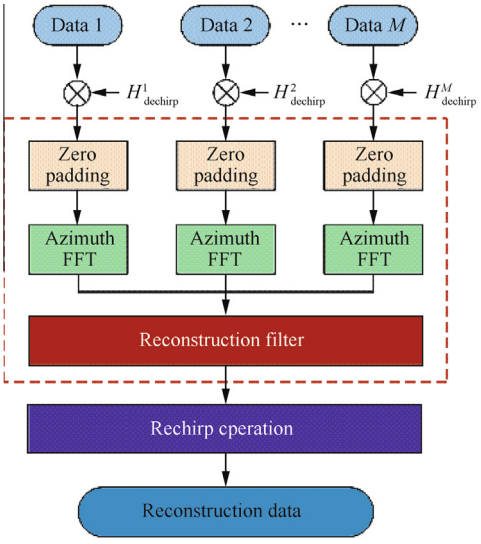

Fig. 3 Flowchart of MPAs data reconstruction process.

where $t^i_{\mathrm{del}} = \frac{d_i}{2v_s}$ denotes the ith channel delay time, the index i indicates the ith channel, and f_d is the Doppler centroid of the raw data.

(2) Filter operationAfter the dechirp Operation, the Filter Operation can be applied as for the MAPs stripmap SAR data. First, zero padding is applied for every channel data, followed by azimuth FFT. Then, effective azimuth spectral reconstruction can be carried out using the method in Ref.[15] with the reconstructed filter $P_i(f)$.

(3) Rechirp operationThe rechirp operation is carried out using the rechirp filter $H_{\mathrm{rechirp}}(t)$ which performs re-sampling in azimuth frequency domain.

$$H_{\mathrm{rechirp}}(t) = \exp(\mathrm{j}\pi k_w t^2) \quad (11)$$

After MAPs data reconstruction, we have several observations.

The sample rate in azimuth becomes f_{PRF}, given by

$$f_{\mathrm{PRF}} = \frac{N_a \cdot k_w}{M \cdot \mathrm{PRF}} \quad (12)$$

where N_a is the point number after zero padding in azimuth. f_{PRF} is a linear function of N_a. In order to avoid azimuth spectrum aliasing, N_a should be selected properly to satisfy $f_{\mathrm{PRF}} > B_{\mathrm{total}}$. The MAPs data are reconstructed without spectral aliasing so that frequency focusing algorithms can be applied.

3.2. Curved orbit correction

The MHRE is introduced to describe the orbit in Section 2. In order to demonstrate its accuracy, simulations are performed. Table 1 shows the selected Keplerian orbit parameters. The scene center is located at the 0 altitude over the WGS-84 ellipsoid. The look angle is 30°. The analyzed point targets are located 5 km away from each other along the range direction. Fig. 4(a) and (b) show the residual phase errors $4\pi\Delta R(t;r)/\lambda$ based on the THRE and MHRE models, respectively, with 0.25 m resolution in azimuth. $\Delta R(t,r)$ is the range error caused by the hyperbolic range equation for describing the curved orbit.

As illustrated in Fig. 4(a), the residual phase error based on the THRE model is more than 30°, which can lead to azimuth broadening and asymmetric sidelobes and degrade the image quality. On the other hand, when the MHRE model is used, there is mainly residual biquadratic phase error which is smaller than 5° as shown in Fig. 4(b). The effect of this residual phase error on image quality can be ignored. These results demonstrate that the proposed MHRE can effectively remove

Table 1 Orbit parameters.

Parameter	Value
Eccentricity	0.0011
Inclination	97.44°
Semi-major axis	7003.819 km
Argument of perigee	90.0°
Ascending node	0°

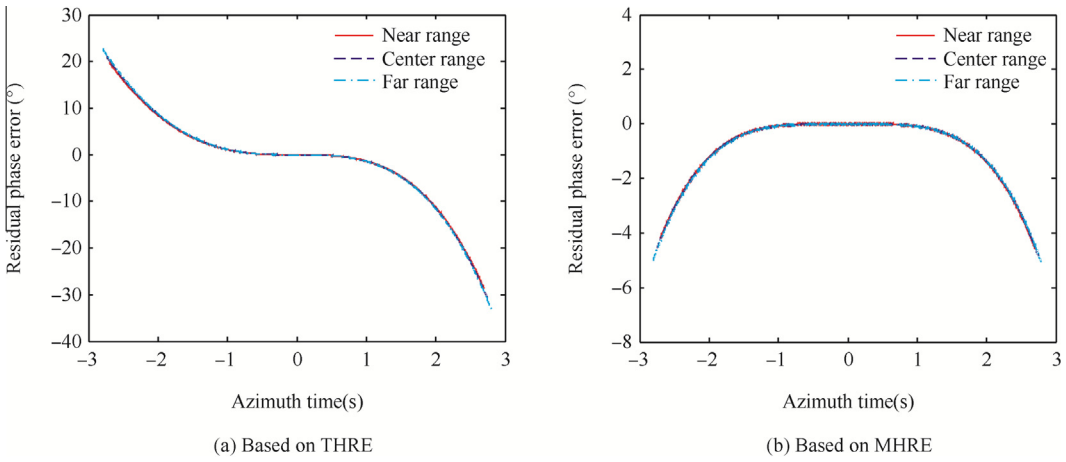

Fig. 4 Residual phase error.

the cubic phase error and provide a better fitting to the actual satellite orbit.

However, there are still two problems to be considered. One is how to calculate the coefficient $\gamma(r)$; the other one is how to compensate the cubic phase error.

Firstly, $\gamma(r)$ can be obtained by the following method. Based on the ephemeris parameters of the satellite, we can acquire the position vector $\boldsymbol{R}_S(t;r)$, the velocity vector $\boldsymbol{V}_S(t;r)$, the accelerated velocity vector $\boldsymbol{A}_S(t;r)$ of the satellite and the position vector $\boldsymbol{R}_T(t;r)$, the velocity vector $\boldsymbol{V}_T(t;r)$, the accelerated velocity vector $\boldsymbol{A}_T(t;r)$ of the point target in Earth-centered Earth-fixed coordinates. So the range $R(t)$ between the satellite and the point target can be calculated by Eq. (13)

$$R(t;r) = |\boldsymbol{R}_S(t;r) - \boldsymbol{R}_T(t;r)| \tag{13}$$

The coefficients $f_0(r),f_1(r),f_2(r),f_3(r)$ can be obtained by a curve fitting operation on the range $R(t;r)$. And $R(t;r)$ can be expressed as

$$R(t;r) \approx f_0(r) + f_1(r)t + f_2(r)t^2 + f_3(r)t^3 \tag{14}$$

The equivalent speed and equivalent angle can be computed by

$$v_r = \sqrt{\frac{\lambda f_0(r) f_2(r)}{2} + \left(\frac{\lambda f_1(r)}{2}\right)^2} \tag{15}$$

$$\varphi_{eq} = \arccos\left(-\frac{\lambda f_1(r)}{2v_r}\right) \tag{16}$$

Then, $\gamma(r)$ can be obtained as follows:

$$\gamma(r) = f_3(r) - \frac{v_r^3}{2f_0^2}\sin^2\varphi_{eq}\cos\varphi_{eq} \tag{17}$$

Note that $\gamma(r)$ is variant with the range and it is very difficult to compensate. However, $\gamma(r)$ can be split into range independent and range dependent components. The range independent component is $\gamma(r_{ref})$, corresponding to the reference range r_{ref}. And the range dependent component is $\Delta\gamma(r) = \gamma(r) - \gamma(r_{ref})$. The range dependent component is so small that it can be neglected in most cases.[8] Therefore, we only focus on the range independent component.

There are two methods to correct phase error for the range independent component: one in the azimuth-time range-frequency domain and the other one in the two-dimensional (2-D) frequency domain. For the first method, we should transform the MAPs data to range frequency domain by range FFT operation; then the correction can be realized by multiplying the data with the following filter in the azimuth-time range-frequency domain.

$$H_{orbit\_1}(t,f_\tau;r_{ref}) = \exp\left[j\frac{2\pi}{3}\frac{\lambda}{c}\gamma(r_{ref})t^3(f_\tau + f_0)\right] \tag{18}$$

where f_τ is range frequency. After multiplication, the data should be transformed to the 2-D time domain by range inverse FFT operation. We can find that both phase and envelope of the signal are changed after correction. The basic idea of this method is to compensate the curved orbit to a straight trajectory; then the MAPs data reconstruction method and traditional algorithms based on the THRE model can be applied without any modification. For the 2-D frequency domain method, we have to obtain the 2-D spectrum of the signal based on the MHRE model. Assume that $t_k(f_\tau,f_t)$ is the stationary point obtained by the principle of stationary phase (POSP). The correction can be realized by multiplying the data with the following filter in the 2-D frequency domain.

$$H_{orbit\_2}(f_t,f_\tau;r_{ref}) = \exp\left(j\frac{4}{3}\pi\gamma(r_{ref})t_k^3(f_\tau,f_t)\right) \tag{19}$$

And

$$t_k(f_\tau,f_t) = \frac{r_{ref}\cos\varphi_{ref}}{v_{ref}} - \frac{r_{ref}f_t\sin\varphi_{ref}}{2v_{ref}^2\sqrt{\left(\frac{1}{\lambda}+\frac{f_\tau}{c}\right)^2 - \left(\frac{f_t}{2v_{ref}}\right)^2}} \tag{20}$$

where φ_{ref} and v_{ref} are equivalent angle and equivalent speed in the reference range, respectively. In a word, both methods can compensate the error caused by the curved orbit validly. The first method is more accurate but less efficient compared with the second one.

3.3. High-order cross-coupling phases compensation

Traditional frequency focusing algorithms make approximations in the 2-D frequency domain, only taking account of the second-order term of cross-coupling phases between azimuth and range.[23,24] However, the impact of the higher-order

cross-coupling phases cannot be ignored in high-resolution applications.

The 2-D Fourier transform of the signal impulse response has the following form

$$S(f_\tau,f_t;r)=\sigma w(f_t)\cdot a(f_\tau)\cdot\exp\{j\psi(f_\tau,f_t;r)\} \tag{21}$$

where $w(f_t)$ is the transform of antenna weighting, and $a(f_\tau)$ the pulse envelope. The phase term $\psi(f_\tau,f_t;r)$ has an exact expression given below:

$$\psi(f_\tau,f_t;r)=-\frac{4\pi r\sin\varphi_r}{\lambda}\sqrt{1-\left(\frac{\lambda f_t}{2v_r}\right)^2}\sqrt{1-\frac{\frac{2f_\tau\lambda}{c}+\left(\frac{f_\tau\lambda}{c}\right)^2}{1-\left(\frac{\lambda f_t}{2v_r}\right)^2}} \tag{22}$$

With Taylor series expansion on the range frequency f_τ, φ_r is equivalent angle in the range, $\psi(f_\tau,f_t;r)$ has the following form

$$\begin{aligned}\psi_i(f_\tau,f_t;r)&=\psi_0(f_t;r)+\psi_1(f_t;r)f_\tau+\psi_2(f_t;r)f_\tau^2\\&\quad+\cdots\psi_i(f_t;r)f_\tau^i+\cdots\end{aligned} \tag{23}$$

where i is the order of the Taylor series expansion. $\psi_i(f_\tau,f_t;r)$ becomes a closer approximation to $\psi(f_\tau,f_t;r)$ as i increases. The residual phase error when we expand Eq. (22) to the ith order can be calculated by

$$\Delta\psi_i(f_\tau,f_t;r)=\psi(f_\tau,f_t;r)-\psi_i(f_\tau,f_t;r) \tag{24}$$

Residual phase errors for $i=3,4$ and 5 are shown in Fig. 5.

We can see that the higher-order cross-coupling phase error is up to 400° at the edge of the bandwidth if Eq. (22) is only expanded to the 3rd order. This residual phase error can lead to a defocused/blurred image. The residual phase errors are less than 20° and 0.2° if Eq. (22) is expanded to the 4th and 5th orders, as shown in Fig. 5(b) and (c), respectively. Therefore, the high-order cross-coupling phase errors have to be compensated to obtain a high image quality. In this case, we only take into account the terms up to the 5th order and ignore the higher order terms. The phase error can be compensated in the 2-D frequency domain by the following phase filter

$$\begin{aligned}H_{\text{couple}}(f_t,f_\tau;r_{\text{ref}})&=\exp\{-j(\psi_3(f_t;r_{\text{ref}})f_\tau^3+\psi_4(f_t;r_{\text{ref}})f_\tau^4\\&\quad+\psi_5(f_t;r_{\text{ref}})f_\tau^5)\}\end{aligned} \tag{25}$$

And

$$\psi_3(f_t;r_{\text{ref}})=-\frac{2\pi\lambda^2 r_{\text{ref}}\sin\varphi_{\text{ref}}}{c^3D^5(f_t)}\cdot\left(\frac{\lambda f_t}{2v_{\text{ref}}}\right)^2 \tag{26}$$

$$\psi_4(f_t;r_{\text{ref}})=-\frac{\pi\lambda^3 r_{\text{ref}}\sin\varphi_{\text{ref}}}{2c^4}\cdot\frac{D^2(f_t)-5}{D^7(f_t)}\cdot\left(\frac{\lambda f_t}{2v_{\text{ref}}}\right)^2 \tag{27}$$

$$\psi_5(f_t;r_{\text{ref}})=\frac{\pi\lambda^4 r_{ref}\sin\varphi_{\text{ref}}}{2c^5}\cdot\frac{3D^2(f_t)-7}{D^9(f_t)}\cdot\left(\frac{\lambda f_t}{2v_{\text{ref}}}\right)^2 \tag{28}$$

$$D(f_t)=\sqrt{1-\left(\frac{\lambda f_t}{2v_{\text{ref}}}\right)^2} \tag{29}$$

However, for higher resolution case, the high-order cross-coupling phase errors are much larger, and higher order terms should be taken into account in Eq. (25). What's more, the phase filter in Eq. (25) is relative to the reference range r_{ref}, which can compensate the high-order cross-coupling phases for targets in the reference range. For targets in range r, there exists residual phase described as

$$\begin{aligned}\Delta\varphi_{\text{couple}}(f_t,f_\tau;r)&=(\psi_3(f_t;r_{\text{ref}})f_\tau^3+\psi_4(f_t;r_{\text{ref}})f_\tau^4\\&\quad+\psi_5(f_t;r_{\text{ref}})f_\tau^5)-(\psi_3(f_t;r)f_\tau^3\\&\quad+\psi_4(f_t;r)f_\tau^4+\psi_5(f_t;r)f_\tau^5)\end{aligned} \tag{30}$$

Note that the residual phase increases with range displacement Δr (defined as $r-r_{\text{ref}}$) from Eq. (30). Fig. 6(a) and (b) show the residual phase for targets in near range and far range, respectively. It can be seen that the maximal residual phase is only about 10°and can be ignored in this case. However, as swath becomes larger and resolution becomes better, the residual phase will correspondingly become larger. To guarantee the image quality in the whole scene, the maximal residual phase should be less than $\pi/4$.

3.4. Doppler parameters updating along azimuth

The chirp scaling (CS) algorithm is an efficient algorithm for updating the Doppler parameters along the range direction. However, it assumes that the Doppler parameters are invariant along the azimuth direction. In reality, they change slightly due to rotation of the Earth and curved orbit. Such variations cannot be ignored for high-resolution and wide-swath SAR systems. To find the variation characteristics of the Doppler parameters along the azimuth direction, the Doppler rates of the point targets with the same closest range located at different azimuth positions are calculated. The simulation parameters are the same as those in Section 3.2. Fig. 7(a) shows the results. We can see that the variation changes almost linearly with the distance to the azimuth center. The largest deviation

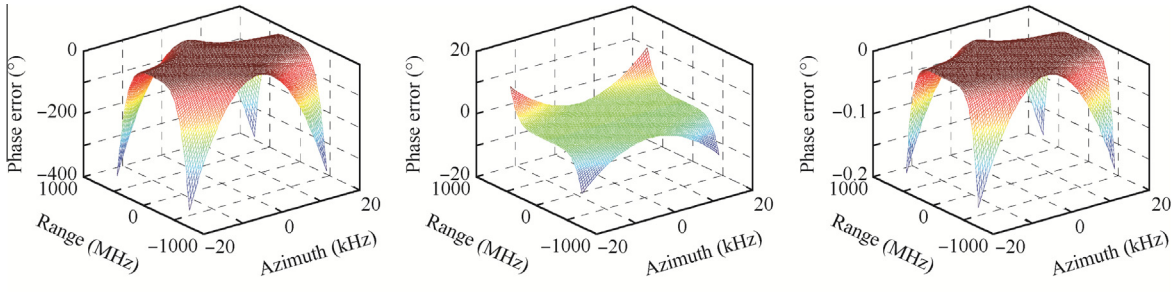

(a) i=3 (b) i=4 (c) i=5

Fig. 5 Residual phase errors in two-dimensional frequency domain.

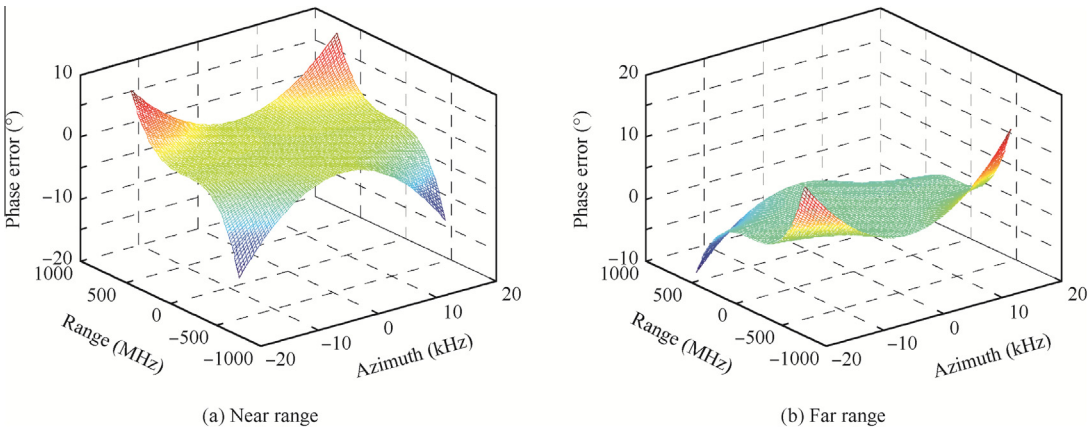

Fig. 6 Residual phase after compensation for targets in near range and far range.

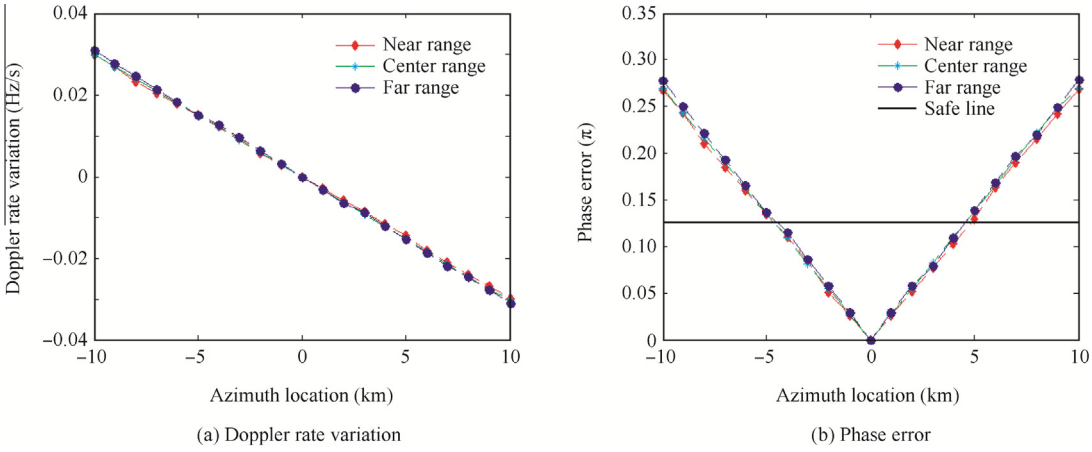

Fig. 7 Variations along azimuth direction.

is up to 0.03 Hz/s at the azimuth edge, yielding about 50° phase error with 0.25 m resolution in azimuth, which can degrade the azimuth resolution. The phase error caused by Doppler rate variation is given in Fig. 7(b).

To guarantee the image quality along the azimuth direction, the data can be processed by azimuth segmentation. In each segment, the Doppler rate variation can be updated correspondingly. The steps are given as follows.

Step 1. Divide the image data into segments along the azimuth direction with maximal phase error caused by Doppler rate variation less than $\pi/8$ (black solid line in Fig. 7(b)).

Step 2. Transform the segment data into range Doppler domain by azimuth FFT operation.

Step 3. Compute the azimuth segment compensation filter $H_{\text{az\_com}}(x_m, r; f_\text{t})$ according to Eq. (31) for each segment, where the azimuth position x_m is updated to the azimuth middle position of each segment, $k_\text{a}(x_m, r)$ and $k_\text{a}(x_0, r)$ are Doppler rates of targets at the position (x_m, r) and the azimuth reference position (x_0, r), respectively. And then, multiply it with the data.

$$H_{\text{az\_com}}(x_m, r; f_\text{t}) = \exp\left\{-\text{j}\pi f_\text{t}^2 \frac{k_\text{a}(x_m, r) - k_\text{a}(x_0, r)}{k_\text{a}(x_m, r) \cdot k_\text{a}(x_0, r)}\right\} \tag{31}$$

Step 4. Transform the data into image domain by azimuth inverse FFT operation.

Then, the segment image data can be combined together and an exact focused image of the whole scene is obtained.

3.5. Summary of the proposed imaging algorithm

A flowchart for our proposed imaging algorithm is shown in Fig. 8. It has four steps: MAPs Data Reconstruction, Data Focusing, Re-sampling Processing and Azimuth Segmenting. The first and third steps are analyzed in detail in Section 3.1 and in Ref.[14], respectively. The proposed algorithm makes some modifications at the second step to compensate the phase errors caused by the curved orbit and high-order cross-coupling phase approximation. The last step is to compensate the phase error caused by the Doppler parameters variation along the azimuth direction. Considering the accuracy and efficiency, the CS algorithm

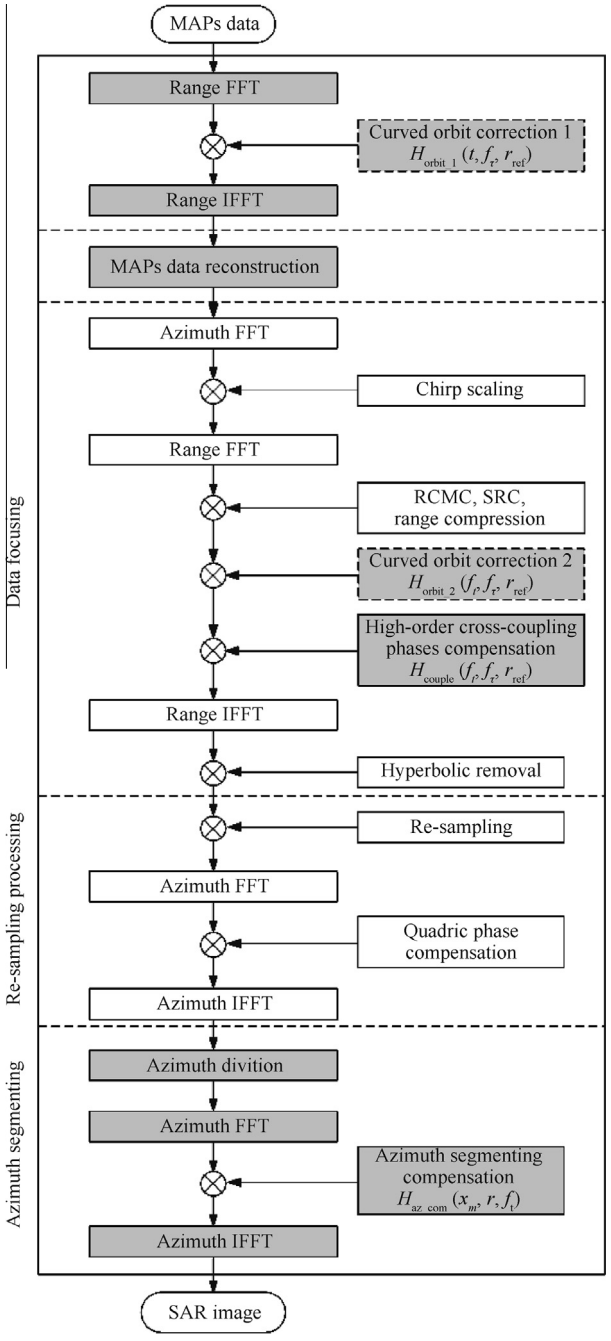

Fig. 8 Flowchart of the proposed imaging algorithm for MAPs-VHR spaceborne sliding spotlight SAR.

is chosen as the imaging algorithm kernel, which implements range cell migration correction (RCMC), range compression, second range compression (SRC), as well as hyperbolic phase removal. Furthermore, some operations are added to the CS algorithm as shown in Fig. 7. The curved orbit correction is applied using the phase filter $H_{\text{orbit\_1}}(t, f_\tau; r_{\text{ref}})$ given by Eq. (18) or $H_{\text{orbit\_2}}(f_t, f_\tau; r_{\text{ref}})$ given by Eq. (19). Moreover, the high-order cross-coupling phases can be compensated in the 2-D frequency domain using the phase filter $H_{\text{couple}}(f_t, f_\tau; r_{\text{ref}})$ given by Eq. (25).

4. Simulation results

Simulations are performed to assess the imaging result of the proposed algorithm for processing the MAPs-VHR spaceborne sliding spotlight SAR data. The required parameters are listed in Table 2. Fig. 9 shows the designed simulation scene. In Fig. 9(a), nine isolated-scatterer points (P_1–P_9) with a uniform spacing of 5 km from each other are included to validate the proposed algorithm in full scene. Also four multi-scatterer points (MS_1–MS_4) are set to analyze the performance of resolution. The multi-scatterer point includes nine points (S_1–S_9) with tight interval of 0.3 m as shown in Fig. 9(b).

The contour plots of the impulse response function (IRF) of the nine isolated-scatterer points are shown in Fig. 10. It can be seen that all of the nine isolated-scatterer points are well focused, although there exist small squint angles of the isolated-scatterer point at the azimuth edges due to azimuth antenna-beam steering in the sliding spotlight mode.

The obtained image quality parameters including impulse response width (IRW), peak sidelobe ratio (PSLR), and integrated sidelobe ratio (ISLR) in both azimuth and range are computed and listed in Table 3, where we can see that all of them are close to ideal values. The broadening of IRW is smaller than 1% in both azimuth and range. Moreover, the changes of IRW in azimuth are observed and the IRW for the isolated-scatterer point at near slant range is better than the one in far slant range.

What's more, to analyze the performance of resolution, Fig. 11 shows the imaging results of multi-scatterer points MS_1. Fig. 11(a) and (b) show the azimuth profile and range profile, respectively. It can be seen that the three points are separated obviously at −3 dB. The contour plot of the IRF of MS_1 is given in Fig. 11(c), and the nine points are well focused. The results indicate that the proposed algorithm has a good performance of resolution.

As a result, both the imaging results of the isolated-scatterer points and multi-scatterer points demonstrate the effectiveness of the proposed imaging algorithm. Furthermore, to show the necessity of curve orbit correction and high-order cross-coupling phases compensation, Fig. 12 gives the contour plots of the IRF for isolated-scatterer points P_1 and P_9 using the CS kernel without any corrections. It can be seen that the IRFs are severely degraded, especially for isolated-scatterer points at the edge of the scene.

Table 2 Simulation parameters.

Parameter	Value
Platform height	514.0 km
Wavelength	0.03 m
PRF	2300 Hz
Bandwidth	1000 MHz
Sample frequency	1200 MHz
Look angle	30.0°
Number of channels	3
Azimuth antenna length	2.6 m

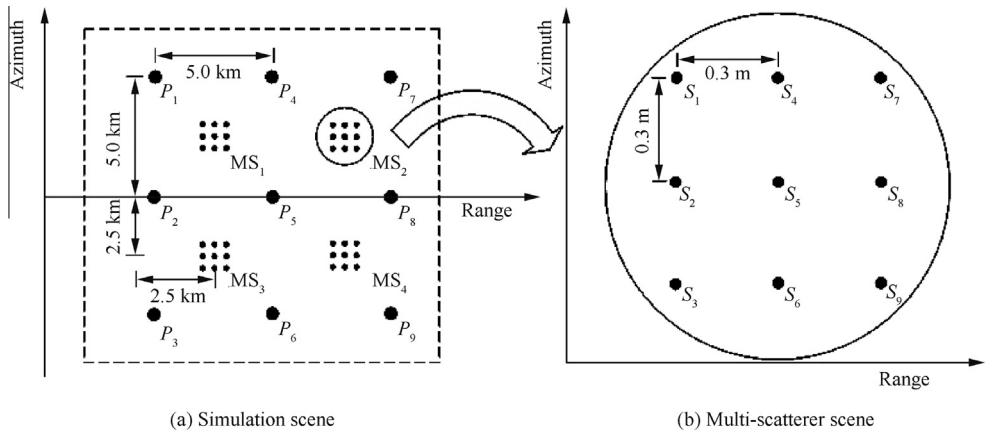

(a) Simulation scene (b) Multi-scatterer scene

Fig. 9 Simulation scene.

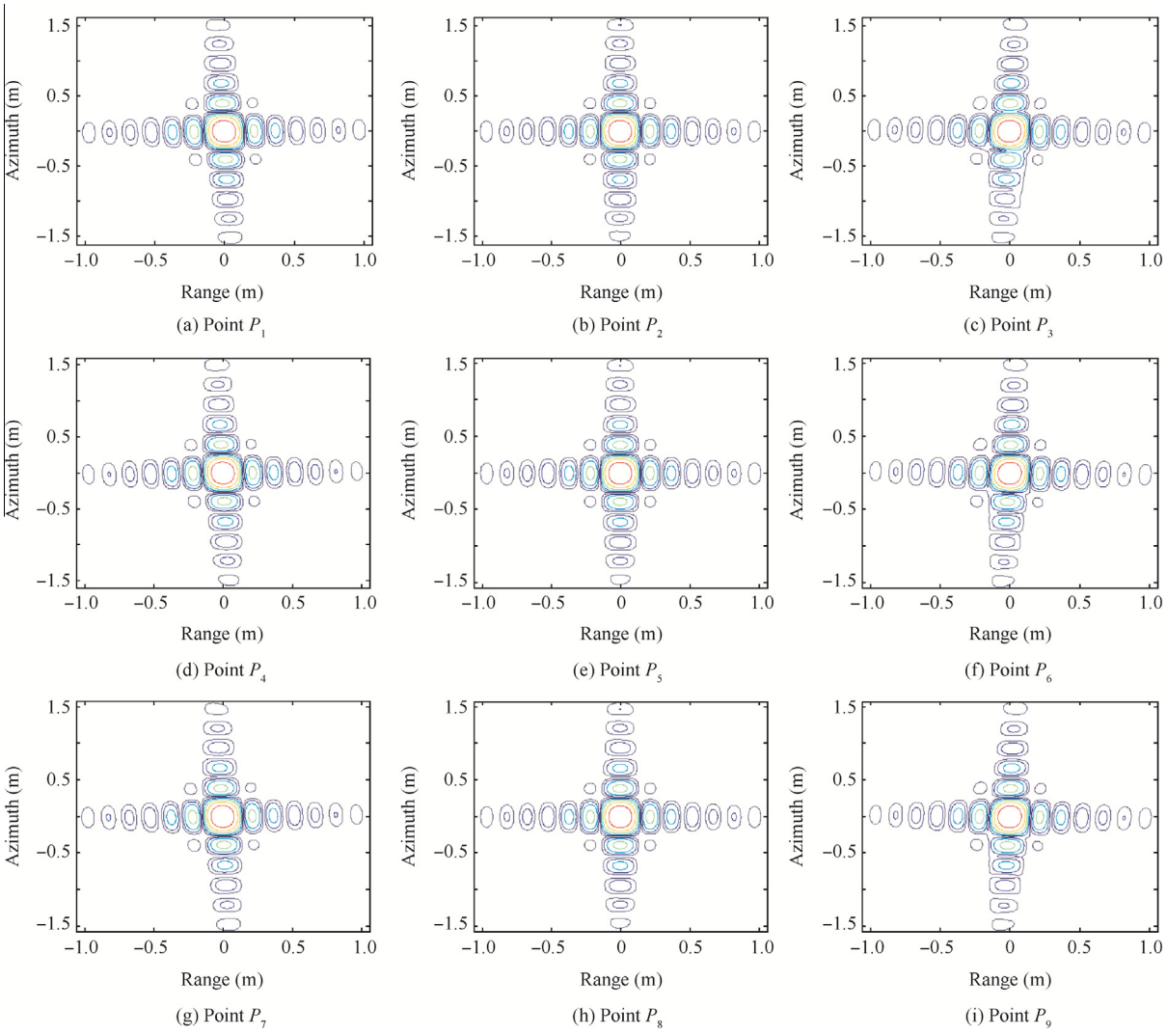

(a) Point P_1 (b) Point P_2 (c) Point P_3

(d) Point P_4 (e) Point P_5 (f) Point P_6

(g) Point P_7 (h) Point P_8 (i) Point P_9

Fig. 10 Contour plots of IRF of isolated-scatterer points.

Table 3 Quality measurement results.

Point	Azimuth			Range		
	IRW(m)	PSLR(dB)	ISLR(dB)	IRW(m)	PSLR(dB)	ISLR(dB)
P_1	0.246	13.264	10.266	0.133	13.129	10.063
P_2	0.246	13.274	10.251	0.133	13.213	10.010
P_3	0.246	13.226	10.306	0.133	13.151	10.097
P_4	0.242	13.238	10.263	0.132	13.071	10.101
P_5	0.242	13.275	10.251	0.133	13.241	10.029
P_6	0.242	13.208	10.292	0.132	13.177	10.123
P_7	0.238	13.265	10.275	0.132	13.034	10.074
P_8	0.239	13.273	10.250	0.133	13.273	10.450
P_9	0.239	13.207	10.287	0.133	13.066	10.113

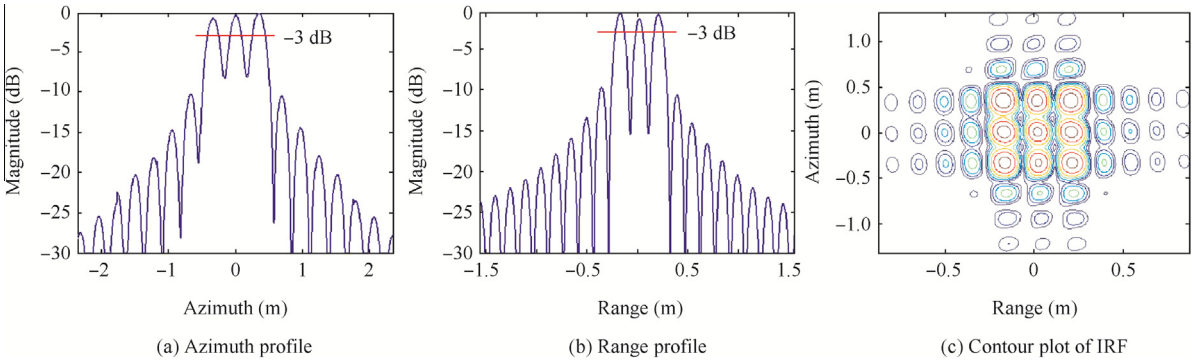

Fig. 11 Imaging results of multi-scatterer points MS_1.

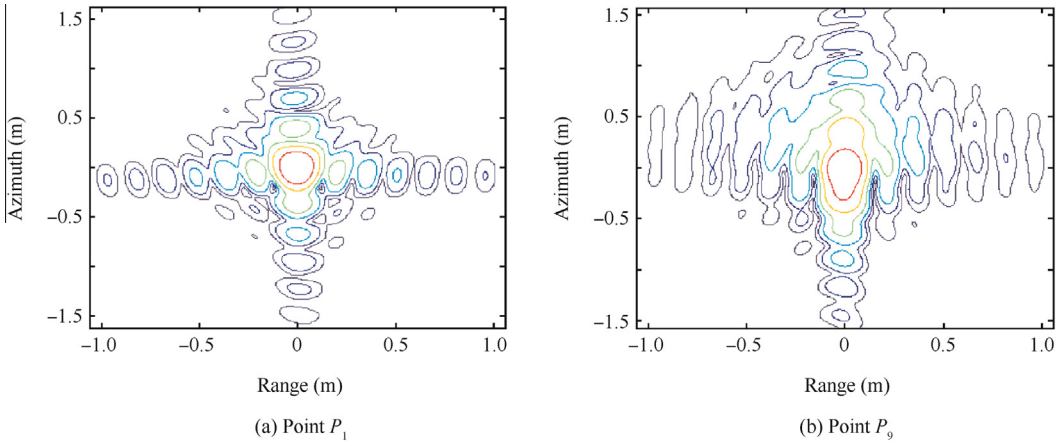

Fig. 12 Contour plots of IRF of isolated-scatterer points without any corrections.

5. Conclusion

Based on the MAPs-VHR spaceborne sliding spotlight SAR system, a new method has been proposed for high-resolution and wide-swath imaging. To improve the performance of the MAPs-VHR spaceborne sliding spotlight SAR system, firstly, the MHRE model is introduced to describe the curved orbit more accurately with the corresponding corrections presented; secondly, to deal with the azimuth spectral aliasing problem when the Doppler bandwidth of the MAPs-VHR SAR data is larger than the equivalent PRF, a data reconstruction method based on the de-rotation operation is proposed; thirdly, to guarantee image quality of the whole scene, the high-order cross-coupling phases are compensated and variations of the Doppler parameters along the azimuth direction are considered. With all these considerations, a novel algorithm for MAPs-VHR sliding spotlight SAR data processing has been proposed based on the previously developed three-

step algorithm. The effectiveness of the proposed method has been verified by simulation results for a scene with isolated-scatterer points and multi-scatterer points.

Acknowledgement

This work was supported by the National Natural Science Foundation of China (No. 61132006).

References

1. Sun GC, Xing MD, Xia XG, Yang J, Wu Y, Bao Z. A unified focusing algorithm for several modes of SAR based on FrFT. *IEEE Trans Geosci Remote Sens* 2013;**51**(5):3139–55.
2. Liu M, Zhang L, Li CL. Nonuniform three-dimensional configuration distributed SAR signal reconstruction clutter suppression. *Chin J Aeronaut* 2012;**25**(3):425–9.
3. Guo J, Xu YS, Fu LS. An extended chirp scaling algorithm for spaceborne sliding spotlight synthetic aperture radar imaging. *Chin J Aeronaut* 2014;**27**(4):892–902.
4. De ZF, Monti GA. TOPSAR: Terrain observation by progressive Scans. *IEEE Trans Geosci Remote Sens* 2006;**44**(9):2352–60.
5. Juergen J, Steffen G, Wolfgang K, Alexander K, Christian F. TerraSAR-X2 – mission overview. *Proceedings of IEEE international geoscience and remote sensing symposium*; 2012 Jul 22–27; Munich, Germany. Piscataway, NJ: IEEE Press; 2012. p. 217–20.
6. Han B, Zhang YJ, Hu DH, Huang LJ. Research on mending of spaceborne sliding spotlight SAR imaging model error. *J Electron Inf Technol* 2011;**33**(7):1694–9 Chinese.
7. Huang LJ, Qiu XL, Hu DH, Ding CB. Focusing of medium-earth-orbit SAR with advanced nonlinear chirp scaling algorithm. *IEEE Trans Geosci Remote Sens* 2011;**49**(1):500–8.
8. Prats-Iraola P, Scheiber R, Rodriguez CM, Mittermayer J, Wollstadt S, De ZF, et al. On the processing of very high resolution spaceborne SAR data. *IEEE Trans Geosci Remote Sens* 2014;**52**(10):6003–16.
9. Luo YH, Zhao BJ, Han XL, Wang R, Song HJ, Deng YK. A novel high-order range model and imaging approach for high-resolution LEO SAR. *IEEE Trans Geosci Remote Sens* 2014;**52**(16):3473–85.
10. Lanari R, Zoffoli S, Sansosti E, Formaro G, Serafino F. New approach for hybrid Strip-map/Spotlight SAR data focusing. *IET Radar Sonar Navig* 2011;**148**(6):363–72.
11. Lanari R, Tesauro M, Sansosti E, Fornaro G. Spotlight SAR data focusing based on a two-step processing approach. *IEEE Trans Geosci Remote Sens* 2001;**39**(9):1993–2004.
12. Prats P, Scheiber R, Mittermayer J, Meta A, Moreira A. Processing of sliding spotlight and TOPS SAR data using baseband azimuth scaling. *IEEE Trans Geosci Remote Sens* 2010;**48**(2):770–80.
13. Mittermayer J, Lord R, Borner E. Sliding spotlight SAR processing for TerraSAR-X using a new formulation of the extended chirp scaling algorithm. *Proceedings of IEEE international geoscience and remote sensing symposium*; 2003 Jul 21–25; Toulouse, France. Piscataway, NJ: IEEE Press; 2003. p. 1462–4.
14. Yang W, Chen J, Zeng HC, Zhou J, Wang PB, Li CS. A novel three-step image formation scheme for unified focusing on spaceborne SAR data. *Prog Electromagnet Res* 2013;**137**:621–42.
15. Krieger G, Gebert N, Moreira A. Unambiguous SAR signal reconstruction from nonuniform displaced phase center sampling. *IEEE Geosci Remote Sens Lett* 2004;**1**(4):260–4.
16. Jing W, Xing MD, Qiu CW, Bao Z, Yeo TS. Unambiguous reconstruction and high-resolution imaging for multiple-channel SAR and airborne experiment results. *IEEE Geosci Remote Sens Lett* 2009;**6**(1):102–6.
17. Li ZF, Wang HY, Su T, Bao Z. Generation of wide-swath and high-resolution SAR images from multichannel small spaceborne SAR systems. *IEEE Geosci Remote Sens Lett* 2005;**2**(1):82–6.
18. Gebert N, Krieger G, Moreira A. Multichannel azimuth processing in ScanSAR and TOPS mode operation. *IEEE Trans Geosci Remote Sens* 2010;**48**(7):2994–3008.
19. Chen Q, Deng YK, Wang R, Liu YD. Investigation of multi-channel sliding spotlight SAR for ultrahigh-resolution and wide-swath imaging. *IEEE Geosci Remote Sens Lett* 2013;**10**(6):1339–43.
20. Sun GC, Xing MD, Xia XG, Wu YF, Huang PP, Wu YR, et al. Multichannel full-aperture azimuth processing for beam steering SAR. *IEEE Trans Geosci Remote Sens* 2013;**51**(9):4761–78.
21. Wang GD. A deramp chirp scaling algorithm for processing spaceborne spotlight SAR data. *Proceedings of microwave and millimeter wave technology*; 2004 Aug 18–21; Beijing, China; Piscataway, NJ: IEEE Press; 2004. p. 659–63.
22. Cumming IG, Wong FH. *Digital processing of synthetic aperture radar data: algorithms and implementation*. Boston: Artech House; 2005. p. 127.
23. Raney RK, Runge H, Bamler R, Cumming IG, Wong FH. Precision SAR processing using chirp scaling. *IEEE Trans Geosci Remote Sens* 1994;**32**(4):786–99.
24. Moreira A, Mittermayer J, Scheiber R. Extended chirp scaling algorithm for air- and spaceborne SAR data processing in stripmap and scanSAR imaging modes. *IEEE Trans Geosci Remote Sens* 1996;**34**(5):1123–36.

Kuang Hui is a Ph.D. student at the school of electronic and information engineering, Beihang University (BUAA). He received his B.S. degree from Beihang University in 2008. His research is signal processing of high-resolution and wide-swath mode in spaceborne SAR.

Chen Jie is a professor and Ph.D. supervisor at the school of electronic and information engineering, Beihang University (BUAA), Beijing, China. He received the B.S. and Ph.D. degrees in information and communication engineering from the same university in 1996 and 2002, respectively. His main research interests include multimodal remote sensing data fusion, topside ionosphere exploration with spaceborne high-frequency/very high-frequency synthetic aperture radar (SAR) systems, high-resolution spaceborne SAR image formation and SAR image quality enhancement.

Yang Wei received the M.S. and Ph.D. degrees in signal and information processing from Beihang University (BUAA) in 2008 and 2011, respectively, and then became a teacher there. His main research interests include ultrahigh-resolution spaceborne SAR image formation, modeling and data simulation and novel techniques for spaceborne SAR systems.

Liu Wei received the B.Sc. degree in space physics (minor in electronics) and the L.L.B. degree in intellectual property law from Peking University, Beijing, China, in 1996 and 1997, respectively; the M.Phil. degree in electrical and electronic engineering from the University of Hong Kong, Pokfulam, Hong Kong, in 2001; and the Ph.D. degree in electronics and computer science from the University of Southampton, Southampton, U.K., in 2003. He is a lecturer in University of Sheffield, Sheffield, U.K. His research interests are mainly in sensor array signal processing, blind signal processing, multirate signal processing and their various applications in wireless communications, sonar, radar, satellite navigation, speech enhancement, and biomedical engineering.